Journal of Metals, Materials and Minerals, 34(4), 2167, 2024

In-situ embedding of nanocylindrical $Bi_{25}FeO_{40}$ into scaffold-C_3N_4 for enhanced Z-scheme photocatalytic degradation

Yile WANG[1,†], Yuhui MA[2,†], Liang CHU[3,*], and Xing'ao LI[1,*]

[1] *Institute of Advanced Materials & School of Materials Science and Engineering & School of Science, Nanjing University of Posts and Telecommunications, Nanjing 210023, China*
[2] *School of Mathematics and Physics, Nanjing Institute of Technology, Nanjing 211167, China*
[3] *Institute of Carbon Neutrality and New Energy, School of Electronics and Information, Hangzhou Dianzi University, Hangzhou 310018, China*

***Corresponding author e-mail**: chuliang@hdu.edu.cn, lixa@njupt.edu.cn
† These authors contributed equally to this work

Received date:
24 September 2024
Revised date:
12 October 2024
Accepted date:
21 October 2024

Keywords:
$Bi_{25}FeO_{40}$;
C_3N_4;
In-situ embedding;
Z-scheme;
Photocatalytic degradation

Abstract

The development of Z-scheme heterojunctions has emerged as an effective approach for boosting the photocatalytic activity. Herein, we fabricated of a direct Z-scheme heterojunction between scaffold-like C_3N_4 and nanocylindrical $Bi_{25}FeO_{40}$, which exhibits enhanced photocatalytic activity and dye adsorption capacity. The in-situ embedding of $Bi_{25}FeO_{40}$ within scaffold C_3N_4 promotes photogenerated carrier separation, leading to an optimized degradation rate of 0.0205 min^{-1} and a contaminant removal efficiency of 85.3%. This work paves a new path for the development of high-efficiency photocatalytic degradation.

1. Introduction

The dyeing industry stands as a vital component of the modern chemical industry, exhibiting remarkable applications across domains such as dyeing, medical treatment, and analysis & identification [1-3]. Nevertheless, the challenge of treating high-concentration organic dye-laden wastewater in an environmentally benign manner has significantly hindered the industry progression. Traditional approaches encompass physical adsorption, membrane separation, ultrasonic methods, photocatalysis, electrocatalysis, and biodegradation [4-15, 53-55]. Among them, membrane separation, electrocatalysis, and ultrasonic techniques are often deemed costly, while biodegradation is significantly influenced by external factors, such as pH value and dye concentration. Consequently, physical adsorption and photocatalysis have emerged as the most prevalent strategies [16-22,50-52].

Graphitic carbon nitride (C_3N_4), a metal-free narrow bandgap semiconductor, boasts remarkable thermal and chemical stability [23-25]. The synthesis process is economical and environmentally benign, which has garnered significant attention in the realm of photocatalysis [24,25]. This material exhibits promising applications in photocatalytic hydrogen evolution and the degradation of pollutants, particularly organic dyes [26-29]. Previous studies have focused on enhancing the photocatalytic performance of C_3N_4 through doping with precious metals or coupling it with perovskite compounds for the degradation of organic dyes [30,31]. However, C_3N_4 composites still grapple with challenges like limited specific surface area, high recombination rates of photogenerated electron-hole pairs, and low quantum efficiency [32]. To address these issues, strategies have been explored to expand the specific surface area of C_3N_4, such as morphological engineering and heterostructuring.

$Bi_{25}FeO_{40}$, an emerging sillenite material with a distinctive body-centered cubic structure, has garnered considerable attention for its significant impact on the photocatalytic degradation of organic dyes [33,34]. Its narrow bandgap, ranging from approximately 1.8 eV to 2.0 eV, surpasses that of $BiFeO_3$ (2.2 eV to 2.7eV), rendering it a promising candidate for photocatalytic applications within the visible light spectrum. However, the large particle size and smooth surface of $Bi_{25}FeO_{40}$, as reported in previous studies [33,35-40], have hindered its potential by limiting its specific surface area and, consequently its photocatalytic performance. The particles prepared via conventional hydrothermal methods typically measure 2 μm to 10 μm in size, impeding efficient compositing with other materials and reducing contact with degraded pollutants. Thus, the morphological regulation of $Bi_{25}FeO_{40}$ becomes paramount to fostering more efficient photocatalytic reactions. From a band structure perspective, $Bi_{25}FeO_{40}$ acts as a suitable p-type semiconductor [38], capable of forming a p-n junction with g-C_3N_4. By embedding $Bi_{25}FeO_{40}$ in situ onto g-C_3N_4, the resultant heterojunctions generate a built-in electric

field that promotes the more efficient separation of photocarriers. This innovative approach significantly enhances the photocatalytic performance of the composite material.

In this study, scaffold-C_3N_4 (s-C_3N_4) and nanocylindrical $Bi_{25}FeO_{40}$ (BFO) heterojunctions were successfully fabricated. The average size of BFO was effectively managed through ultrasonic treatment of its precursors. Notably, the integration of these two materials into a binary BFO/s-C_3N_4 Z-scheme heterojunction significantly boosted the efficiency of photocatalysis. Additionally, the negative potential of s-C_3N_4 facilitated the adsorption of methylene blue (MB) onto its surface. Remarkably, upon optimizing the ratio of s-C_3N_4 to BFO within the heterojunction, the degradation efficiency underwent a substantial enhancement subsequent to MB adsorption. This study introduces a novel photocatalyst with immense potential for environmental remediation in practical applications and presents a green technology for the synthesis of diverse heterogeneous materials.

2. Experimental section

2.1 Material

Bismuth nitrate pentahydrate ($Bi(NO_3)_3·5H_2O$), ferric chloride hexahydrate ($FeCl_3·6H_2O$), nitric acid (HNO_3), ammonium hydroxide ($NH_3·H_2O$), sodium hydroxide (NaOH), dicyandiamide (DCDA, $C_2H_4N_4$), sodium chloride (NaCl) and methylene blue ($C_{16}H_{18}ClN_3S$) were procured from Shanghai Aladdin Industrial Corporation. All of the chemical reagents mentioned above were analytical grade and used without any other treatment.

2.2 Preparation of scaffold-C_3N_4

For the synthesis of scaffold-C_3N_4 (s-C_3N_4), a NaCl template-assisted growth method was used with a little modification [41]. 0.03 mol DCDA and 0.3 mol NaCl was added into 100 mL deionized water, and the solution was heated at 80°C for 10 min with magnetic stirring. The hot solution was then transferred to the refrigerator immediately for quick cooling. After being stored for 12 h in the refrigerator, the frozen solution was dehydrated by freeze-drying for 24 h to obtain the fluffy white powder. The powder was calcined at 550°C for 2 h under N_2 protection after being transported to the Muffle furnace. The obtained yellow powder was washed several times by means of suction filtration and then dried to obtain the s-C_3N_4.

2.3 Preparation of BFO and BFO/s-C_3N_4 photocatalysts

BFO was fabricated by a typical hydrothermal process. 5 mmol $Bi(NO_3)_3·5H_2O$ and 5 mmol $FeCl_3·6H_2O$ were dissolved into 10 mL HNO_3 with the concentration of 10 M under magnetic stirring. Deionized water (50 mL) was added into form a bright yellow-green solution. Then the $NH_3·H_2O$ was tardily dropped into the solution until reddish-brown precipitation was produced. The whole reaction system was treated in ultrasonic bath for 30 min and 1 h, then wash to neutral with deionized water. The same mass of precursors without ultrasonic treatment were prepared as controls. Finally, the reaction products were transferred into a 40 mL Teflon reactor and 2 M NaOH was added to 75% liquid level height. The autoclave was heated in an oven at 160°C for 24 h. After washing the products with deionized water and ethanol alternately for several times and drying at 60°C for 6 h, the brownish red BFO was obtained. 10 mg BFO and 20 mg s-C_3N_4 were dispersed in 5 mL ethanol and sonicating for 3 min. After dring the suspension, photocatalyst C20B10 was obtained. For comparison, C15B15 and C10B20 were synthesized by the same method with the corresponding feed ratios.

2.4 Analyses of photocatalysts

The samples were characterized by X-ray diffraction (XRD, Bruker D8 Advance), Scanning electron microscope (SEM, Hitachi S-4800) equipped with Energy dispersive spectrometer (EDS), Transmission electron microscope (TEM, Hitachi HT-7800), Zeta potential analyzer (Micromeritics, NanoPlus), X-ray photoelectron spectroscopy (XPS), Photoluminescence (PL), Ultraviolet and visible ultraviolet (UV-vis, PerkinElmer Lambda 35), Automatic surface area and porosity analyzer (BET, Micromeritics APSP 2460). The photocurrent spectra were measured by a solar simulator combined with a Keithley 2400 Source Meter.

2.5 Photocatalytic degradation of MB

Photocatalytic degradation was carried out under a 300 W xenon lamp equipped with a cut-off filter (420 nm). 20 mg photocatalyst was added into 40 mL aqueous solution of MB (20 $mg·L^{-1}$). The mixture of catalyst and dye solution was under continuously magnetic stirred in dark for more than 2 h. Visible radiation reaction begins after adsorption-desorption equilibrium. 4 mL solution was collected every 15 min for centrifugation. The variation of absorption spectra was recorded by the UV-vis within the range of 400 nm to 800 nm.

3. Results and discussion

3.1 Regulation of the morphology of catalysts

The overall preparation process was explained in Figure 1. After the $Bi(NO_3)_3·5H_2O$ and $FeCl_3·6H_2O$ were fully dissolved in nitric acid, whether the product is treated by ultrasonic as an important factor to regulate the morphology of BFO. As mentioned above, three durations were used for comparison. Nanocylindrical BFO was obtained as the final product. Meanwhile, the synthesis of scaffold-C_3N_4 also provides an advantageous carrier for the loading of BFO.

The morphology of the products was analyzed by SEM, TEM and EDS. Benefited from the ultrasonic treatment of the precursors, the BFO prepared by hydrothermal method has a uniform cylindrical nano-structure and overall dimensions of 300 nm to 400 nm. Significantly smaller than the average size of the usual BFO particles. The size of the control group without ultrasonic treatment reached 10 μm, which was close to the average size of previous reports (Figure 2(a)). With the increase of ultrasonic treatment time, the average particle size of BFO samples obtained after hydrothermal reaction decreased continuously. After sonicating the precursor for 30 min, the obtained BFO with nanocylindrical morphology was loaded on the BFO in the

shape of a large square (Figure 2(b)). As the treatment time reaches 1 h, the average size of BFO was greatly reduced, most of them were uniformly dispersed nanocylindrical morphology. (Figure 2(c-d)). Meanwhile, as shown in Figure 2(e-f), the s-C_3N_4 synthesized by freeze-drying NaCl-assisted template method has cavernous scaffold structure with a smooth surface and an aperture of about 5 μm. This is very close to the morphology of the precursors containing NaCl before washing (Figure S1). The BFO and s-C_3N_4 were then ultrasonically compounded in alcohol and dried. A large amount of BFO nanoparticles was anchored in the pores of s-C_3N_4 (Figure 2(g)), which was also shown in the TEM images (Figure 2(h-i)). The EDS results indicate that the Bi, Fe and O were uniformly distributed on the entire surface of the s-C_3N_4/BFO composites (Figure S2). Hence, the BFO were successfully attached to the s-C_3N_4.

3.2 Characterization of photocatalysts

3.2.1 Phase analysis

All XRD patterns were performed in the range of 20° to 60° (Figure 3). For s-C_3N_4, a broad peak at 27.1° corresponding with (002) plane shows the aromatic systems of graphitic stacking [41]. As for BFO, all the peaks correspond well to the standard comparison card (JCPDS No. 46-0416). The diffraction peaks 2θ=27.5° and 32.7° corresponds to (310) and (321) planes, respectively. Indicating that a pure phase $Bi_{25}FeO_{40}$ has been successfully synthesized. Compared with the pure s-C_3N_4 and BFO, the XRD pattern of C20B10 appear as the characteristic peaks of both s-C_3N_4 and BFO.

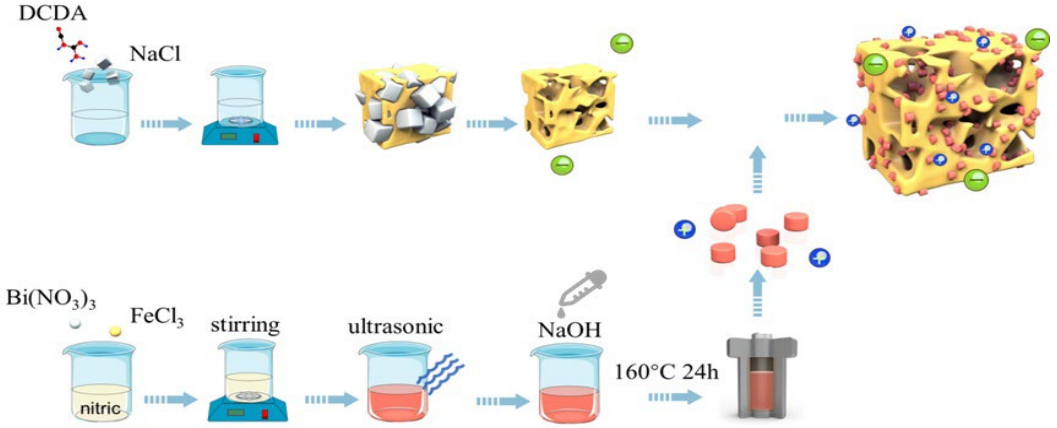

Figure 1. Schematic illustration of synthesis process for BFO/s-C_3N_4 composites.

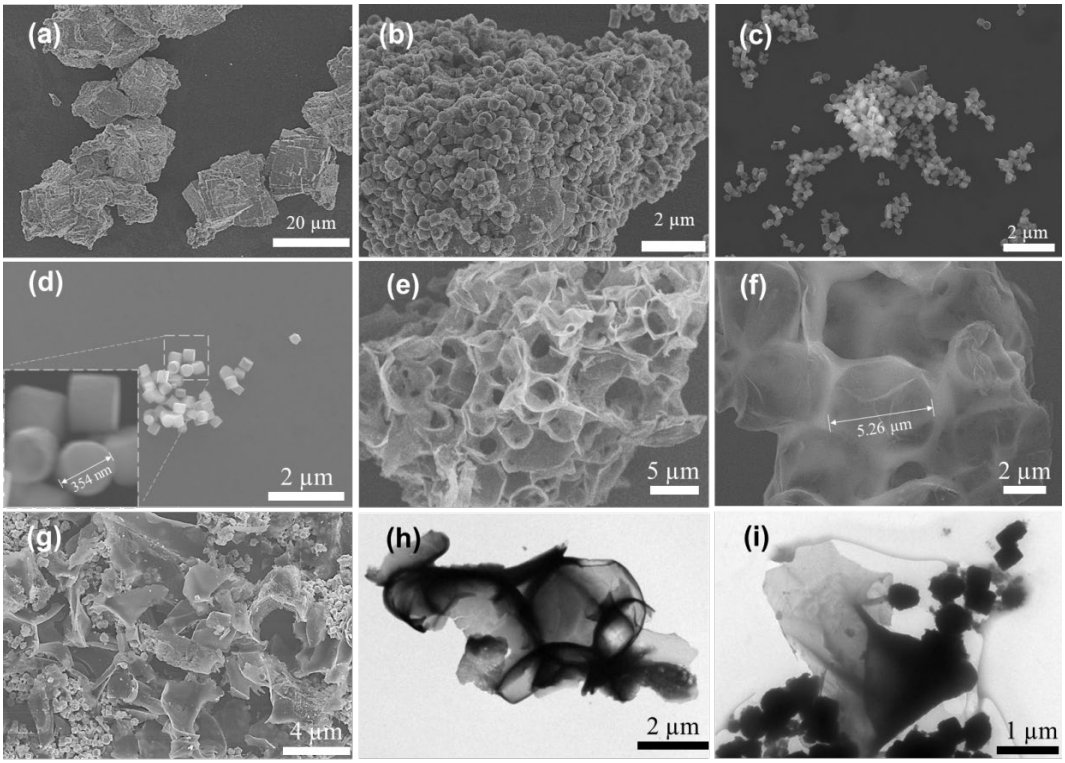

Figure 2. SEM images of BFO obtained through different ultrasonic times: (a) 0, (b) 0.5, (c) 1 h, (d) Enlarged SEM image of BFO, (e-f) SEM images of s-C_3N_4, (g) SEM image s-C_3N_4/BFO heterostructure, TEM images of (h) s-C_3N_4, and (i) s-C_3N_4/BFO heterostructure.

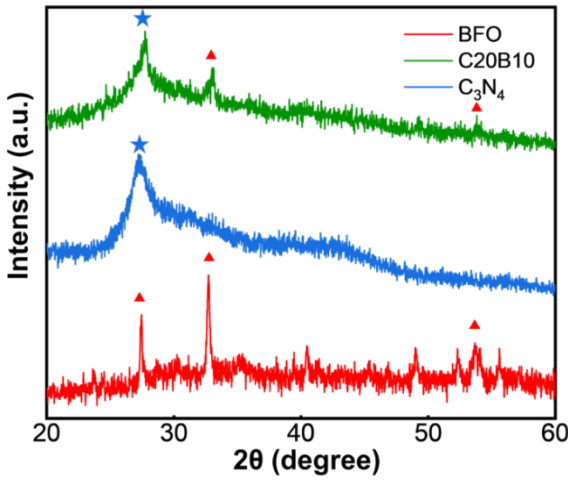

Figure 3. XRD patterns of s-C_3N_4 (blue), BFO (red) and C20B10 (green). The blue star and the red triangle indicate the characteristic peak positions of s-C_3N_4 and BFO, respectively.

3.2.2 Zeta potential and surface area

Zeta potential is the potential difference between the bulk solution and the shear plane, which is always deemed as an indicator for the surface charge of solid particles [42]. The Zeta potential values of three selected samples were shown in Figure 4(a). The Zeta potentials of s-C_3N_4, BFO are –26.58 eV and 15.10 eV, respectively, which is consistent with previous studies [25,42,43]. This means the nano-cylindrical $Bi_{25}FeO_{40}$ could be embedded into scaffold-C_3N_4 by Coulomb force. C20B10 possesses a less negative Zeta potential of –8.35eV, suggesting that the hybridization of s-C_3N_4 with BFO has a significant impact on its surface charge. This also confirms that the internal mechanism of ultrasonic composite of the two samples comes from electrostatic adsorption. As the organic group of MB shows positive potential, the composite catalysts with negative potential is more suitable for the adsorption of MB [44].

As shown in Figure 4(b), with the increasing proportion of BFO, the specific surface area of the complex increases. The specific surface area of pure BFO is 36 $m^2 \cdot g^{-1}$, which is several times larger than that of previous studies [33,45]. The larger specific surface area is conducive to the more uniform adhesion of BFO to s-C_3N_4, which contributes to the improvement of photocatalytic efficiency.

3.2.3 Band structure

In order to study the photocatalytic properties of s-C_3N_4 and BFO, Ultraviolet and visible ultraviolet (UV-vis) spectroscopy measurements were performed on all samples, which were shown in Figure 5(a). The spectra of BFO revealed significant absorption at the range from 400 nm to 800 nm, suggesting that BFO can absorb remarkable amounts of visible light [46]. As the content of s-C_3N_4 in the composites increases, catalysts show stronger intrinsic absorption band at 560 nm. The band gap energies (E_g) about pure s-C_3N_4 and BFO were calculated according to the following Kubelka-Munk formula:

$$\alpha h\nu = A(h\nu - E_g)^{n/2}$$

Where α, *h*, ν, and A are the absorption coefficient, Planck constant, frequency, and proportionality constant, respectively. The n values of s-C_3N_4 (indirect semiconductor) and BFO (direct semiconductor) are 4 and 1, respectively [28,47]. As presented in Figure 5(b-c), the E_g values of s-C_3N_4 and BFO were 2.42 eV and 1.80 eV, respectively, which was resembled to the corresponding results in previous reports [25,48]. Moreover, the XPS are applied to determine the valence band (VB) edges as shown in Figure 5(d). Thus, the VB positions of BFO and s-C_3N_4 are 2.63 eV and 2.06 eV, respectively. According to the corresponding band gap and VB band potential, the conduction band (CB) can be deduced in Figure 5(e). Obviously, ascribing to their narrow band gaps, both s-C_3N_4 and BFO could absorb photon energy under visible light irradiation and thus be stimulated to achieve band-to-band transition. Moreover, the PL spectrum was tested to further study the transfer and recombination of electrons and holes in composites (Figure 5(f)). Stronger emission intensity corresponds to faster electron-hole pair recombination. When the excitation wavelength was 378 nm, all samples showed characteristic PL peak of C_3N_4 at about 450 nm, which was due to the recombination of photogenerated carriers. The decrease of the PL peak intensity indicated that s-C_3N_4 and BFO had formed a heterojunction, which led to the decrease of the recombination probability of photogenerated carriers. A shift in the PL peaks could be found in the PL spectra. This shift in the PL peaks could be attributed to the establishment of the heterojunction. The original energy levels of C_3N_4 were changed by the establishment of the heterojunction, which leads to the shift in the PL peaks.

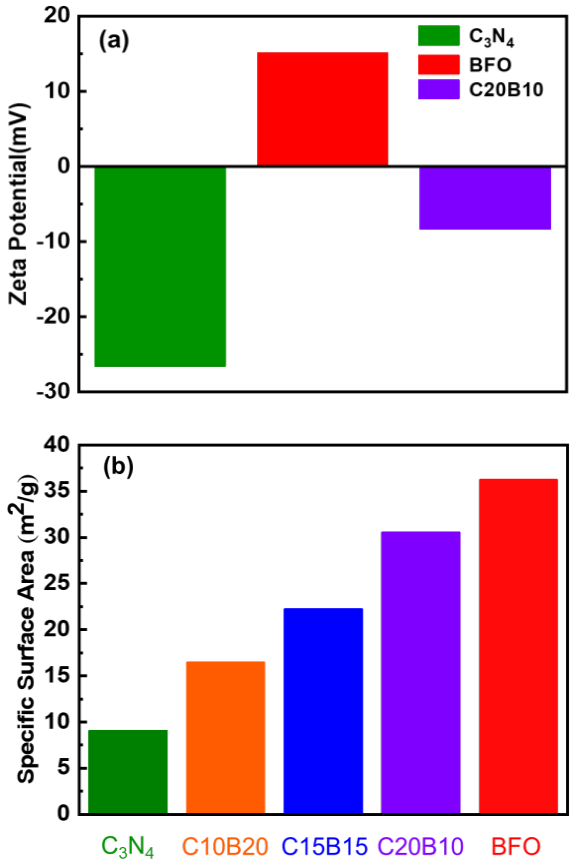

Figure 4. (a) Zeta potential and (b) specific surface area of the as-prepared catalysts.

3.2.4 Photocurrent

To further understand the role of s-C_3N_4/BFO heterojunction, the charge transport efficiencies of different samples were investigated by transient photocurrent (Figure 6(a)). In general, charge carrier density and charge mobility are the key parameters to evaluate the charge transport efficiency. An enhanced photocurrent means a more efficient charge transfer and a slower recombination of electrons and holes, which is beneficial to relevant photocatalytic activity. As indicated in Figure 6(a), the photocurrent density of the C20B10 sample is 0.51 μA·cm^{-2}, which is larger than that of the pure s-C_3N_4 (0.47 μA·cm^{-2}) and pure BFO (0.44 μA·cm^{-2}) samples, respectively. The higher photocurrent density of C20B10 indicates more efficient photogenerated electrons and holes separation and less recombination of the charge carriers at their interface. This is in accordance with the results of PL spectra, which could be attributed to the establishment of heterojunction between C_3N_4 and BFO.

3.3 Photocatalytic performance

3.3.1 Photocatalytic degradation of MB

The photocatalytic performance of all prepared catalysts was tested by degradation of a representative contaminant MB which exhibits the λ_{max} of about 665 nm [49]. Figure 6(b) shows the degradation of MB aqueous solution in the presence of C20B10 sample. It can be clearly drawn from the picture that the UV-vis absorption peak decreased significantly after dark adsorption and photocatalytic reaction. The degradation effects of all tested samples and their corresponding UV-vis spectra were shown in Figure S3. The results illustrate that our sample has outstanding performance in both adsorption and degradation.

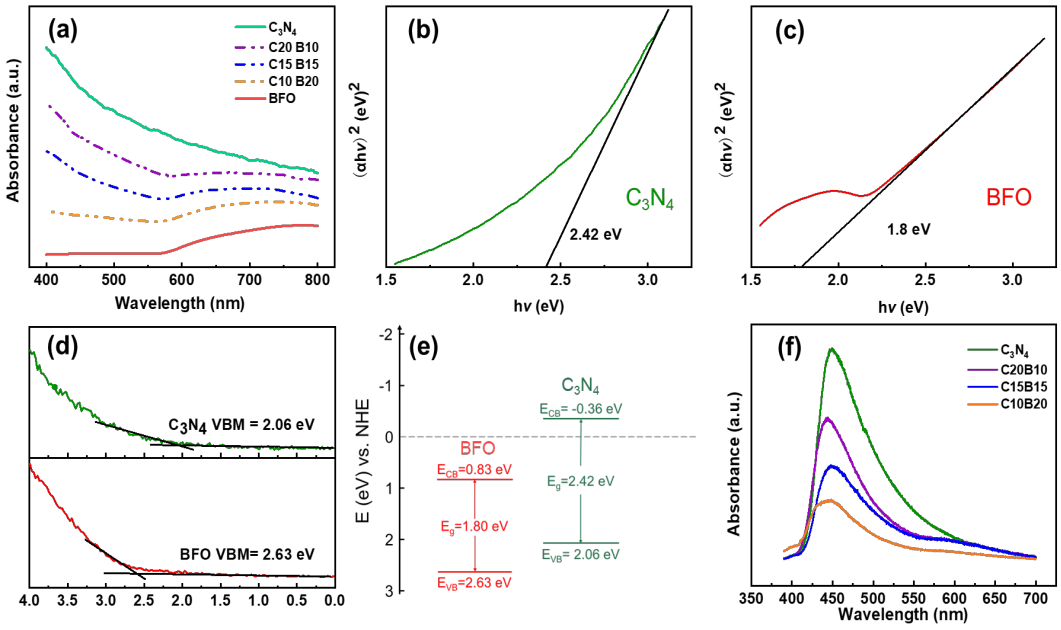

Figure 5. (a) UV–vis spectra, (b-c) Kubelka-Munk transformed function of s-C_3N_4, BFO, (d) Valence band XPS results, and (e) Band structure of s-C_3N_4 and BFO, and (f) Photoluminescence (PL) of pure C_3N_4 and the composites.

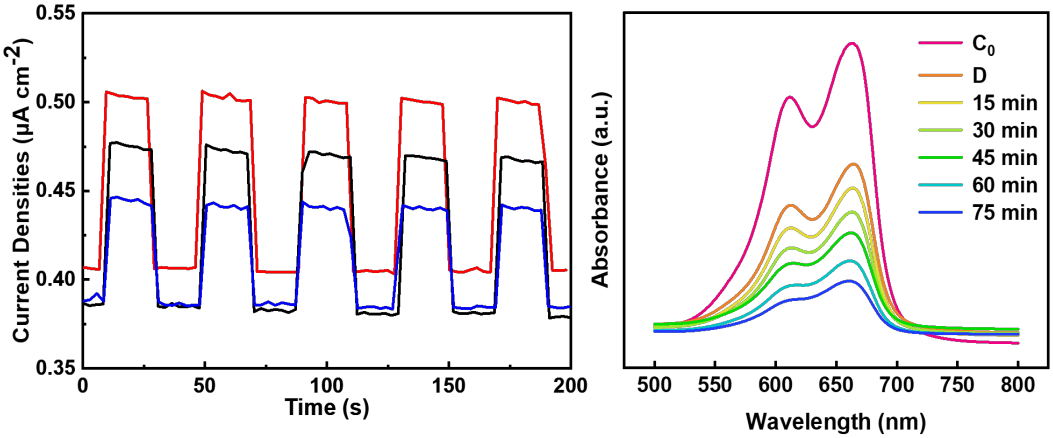

Figure 6. (a) The photocurrent curves of C20B10 (red), s-C_3N_4 (black) and BFO (blue) (b) UV-vis spectra of MB during the whole treatment process in the presence of C20B10.

3.3.2 Effect of composition ratio

The above results can confirm that composite of s-C_3N_4 and BFO has good adsorption and catalytic properties. To further study the factors affecting these properties, pure s-C_3N_4, BFO, and hybrids materials with different components (C10B20, C15B15, C20B10) were prepared to the same photocatalytic reaction. As shown in Figure 7(a), it is obvious that all reaction systems reach adsorption-desorption equilibrium in 1 h under continuous magnetic stirring. The exact amount of MB adsorbed by the catalyst can be calibrated by the following formula:

$$Q_e = \frac{(C_0 - C)V}{m}$$

where Q_e (mg·g^{-1}) stands for to the actual mass of dye adsorbed per gram of catalyst during unit time (1 h), C_0 and C represent the initial and real-time concentrations of dyes. V and m correspond to the volume of solution and the mass of catalyst added in respectively. The adsorption capacity of pure BFO was the weakest among all the samples (Figure 7(b)). After continuous stirring for 1 h in the dark, the Q_e of BFO was only 6.174 mg·g^{-1}. At the same time, pure s-C_3N_4 and composites show higher adsorbability, the maximum adsorption capacity C20B10 reaches 21.562 mg·g^{-1}, which is more than three times that of BFO. This is consistent with the results of the Zeta potential obtained above. In the MB solution, the organic functional groups that cause pollution mainly possesses the positive potential [44]. It is more favorable to attach to the surface of s-C_3N_4. The effective adsorption sites on the surface of s-C_3N_4 decrease with the increase of BFO proportion in composite samples, resulting in weakening adsorption of MB for C10B20 samples.

The photocatalytic performance of catalysts aqueous was estimated by perform photocatalytic degradation of MB under the irradiation of visible light. The reaction rate constant k was obtained from the formula:

$$\ln\frac{C_0}{C} = kt$$

The relationship between ln (C_0/C) and t was summarized in Figure 7(c). Compared with the concentration at adsorption equilibrium, the concentration of the MB decreased to 43.9% (BFO), 52.7% (s-C_3N_4), 61.2% (C10B20), 66.3% (C15B15), and 68.6% (C20B10) respectively in 1 h. It can be inferred from the results that the structure of heterojunction significantly improves the photocatalytic performance. The reaction rate constant k is acquired by linear fitting of the data (Figure 7(d)). The calculated degradation rates were 0.84 × 10^{-3} min^{-1}, 1.18 × 10^{-3} min^{-1}, 1.43 × 10^{-3} min^{-1}, 1.83 × 10^{-3} min^{-1}, and 2.05 × 10^{-3} min^{-1} for BFO, s-C_3N_4, C10B20, C15B15 and C20B10, respectively. For the compound of C20B10, they not only display the excellent adsorption performance, but also show the best performance in photo-catalytic degradation reaction. Considering the previous adsorption process, 85.3% of the dye was removed during a complete reaction cycle.

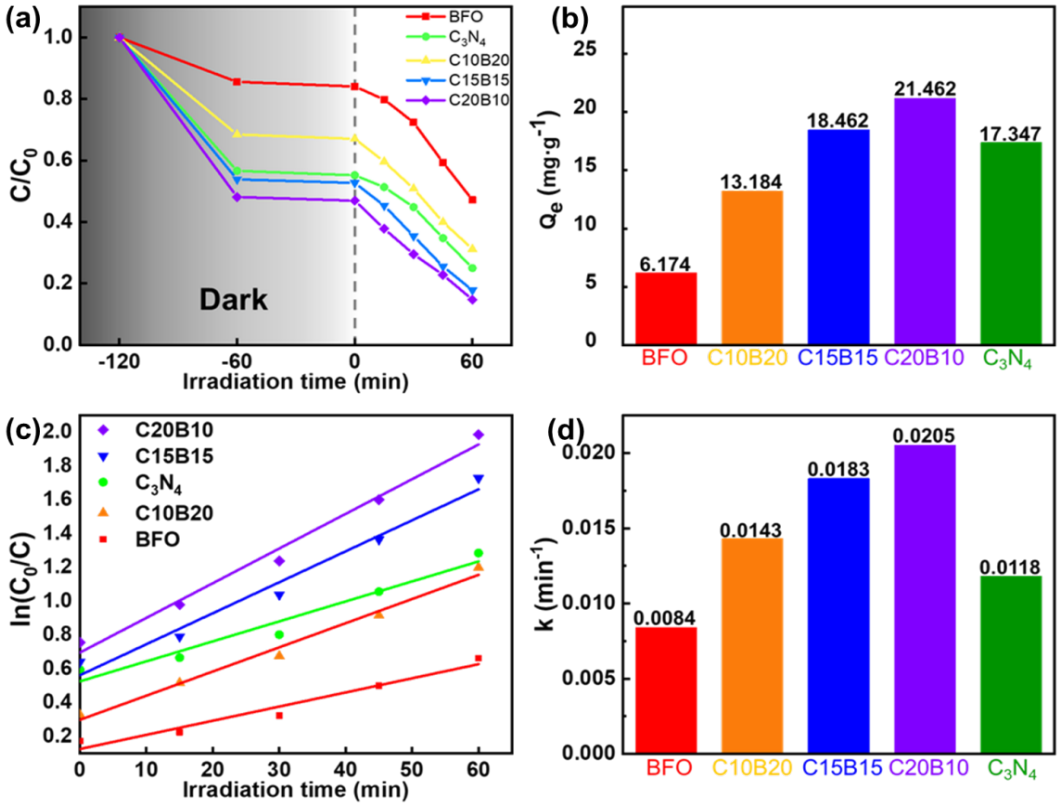

Figure 7. (a) Removal efficiencies of MB by as-prepared samples. (b)Adsorption capacity after the reaction system reaches adsorption/desorption equilibrium. (c) Kinetic analysis of MB degradation under the irradiation of visible light and (d) the corresponding kinetic constants by all samples.

3.3.3 Recyclability and stability

As for catalysts, the recyclability and stability of catalysts are very important as well as the catalytic performance. Each cyclic reaction was carried out under the same visible light irradiation. Consistent with the conditions the previous degradation reaction. 20 mg C20B10 was added into 40 mL aqueous solution of MB (20 mg·L^{-1}). At the end of each reaction, the reaction system was collected without washing process. It is worth mentioning that the BFO in the composite catalyst has strong ferromagnetism [45], which helps to recover the catalyst from the reaction solution (Figure S4). The gathered catalyst was then added to the same concentration and volume of MB aqueous solution for the next reaction cycle. The time-dependent degradation efficiency was depicted in Figure 8. In the initial degradation reaction, the catalyst has reached the adsorption equilibrium and there is an inevitable loss of trace amounts during each catalyst transfer. Hence, with the increase of the cycles number, the adsorption capacity decreases rapidly and the degradation rate also reduces slightly. This could be attributed to the adsorption-desorption equilibrium of the catalysts, because the sample was collected without washing process.

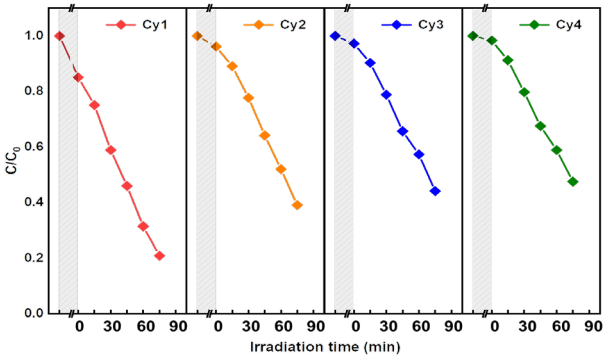

Figure 8. Cycling tests of C20B10 catalysts. The gray diagonal area represents the dark adsorption process.

3.4 Dye removal mechanism

3.4.1 Source of adsorption

It is widely approved that specific surface area and surface charge are two critical factors determining the adsorptive behavior. From the aspect of electrostatic attraction, the surface potential of s-C_3N_4/BFO heterojunction was still suitable for the adsorption of MB. As listed in Table 1, the efficiency of degradation was promoted after the composite of BFO, the increase of BFO makes the surface potential of the heterojunction less negative, limiting the capacity of surface adsorption. After forming a heterojunction, the more dyes are adsorbed, the faster the subsequent degradation rate reaches, indicating that the adsorption of dye on the surface can signally enhance the pollutants degradation efficiency of heterojunction.

3.4.2 Photocatalytic degradation mechanism

The photocatalytic degradation mechanism of MB by s-C_3N_4/BFO composite was investigated. From the above-mentioned XPS results, the VB of s-C_3N_4 and BFO were 2.06 eV and 2.63 eV. CB position of s-C_3N_4 and BFO can be calculated according to the formula:

$$E_{VB} = E_{CB} + E_g$$

The E_g of s-C_3N_4 and BFO acquired from UV−vis measurement were 2.42 eV and 1.80 eV, and the corresponding CB are –0.36 eV and 0.83 eV. Generally, two possible charge transfer modes can be used as photocatalytic mechanisms for heterojunction photocatalysts. One would be supposed to be the traditional type II. The electrons and holes of s-C_3N_4 and BFO were separated under visible light irradiation. Then the photogenerated electrons shift from the CB of s-C_3N_4 to the CB of BFO. The holes in the VB of BFO should be transferred to the VB of s-C_3N_4 directly. Another possible path way for the photo-generated charge carriers was the so-called Z-scheme system. After the separation of electrons and holes by visible light radiation, the electrons in BFO quickly transfer to the VB of s-C_3N_4 and combining with the photoinduced holes. Leading to the accumulation of e^- in the CB of s-C_3N_4 and h^+ in the VB of BFO. However, the CB (0.83 eV) of BFO is less negative than the $\bullet O_2^-$ (–0.33 eV), causing that the O_2 cannot be reduced by electrons in the CB of BFO. Meanwhile, the VB of s-C_3N_4 is negative than OH^-/•OH, which means OH^-cannot be oxidized effectively by the holes generated by s-C_3N_4. By adding different free radical trapping agents into the photocatalytic degradation system, the main active species can be determined. To verify the active species that plays a major role in the catalytic process, 1 mmol of p-benzoquinone (BQ), ethylenediamine tetraacetic acid disodium salt (EDTA-2Na) and isopropyl alcohol (IPA) were used as the scavenger of $\bullet O_2^-$, h^+ and •OH, respectively. A degradation reaction system without any sacrificial agent was set up as a control. The concentration of catalysts and dye was consistent with the recyclability experiment. Figure 9 shows the changes of photocatalytic performance of s-C_3N_4/BFO after adding different trapping agents. The degradation rate was obtained by dividing the amount of degradation by the amount of degradation without the addition of any scavenger. The additions of BQ, IPA and EDTA-2Na limit the efficiency of photocatalytic reaction.

Table 1. Comparison of adsorption capacity and catalytic performance.

	Specific surface area ($m^2 \cdot g^{-1}$)	Adsorption capacity ($mg \cdot g^{-1}$)	Degradation rates ($\times 10^{-3}$ min^{-1})	Total MB removal (L_4/C_0) (%)
p-C_3N_4	9.100	17.347	1.18	74.99
C20B10	16.474	**21.462**	**2.05**	**85.28**
C15B15	22.264	18.462	1.83	82.24
C10B20	30.549	13.184	1.43	72.58
BFO	**36.265**	6.174	0.84	52.85

The degradation rate was only 46.6%, 67.5% and 80.3% of the control group. This result confirms $•O_2^-$, •OH and h^+ plays a key role in the degradation process. Hence the type II systems is not suitable here and the Z-scheme system is a more reasonable explanation for the s-C_3N_4/BFO photocatalytic degradation system (Figure10).

$$s\text{-}C_3N_4 + hv \rightarrow h^+_{VB}(s\text{-}C_3N_4) + e^-_{CB}(s\text{-}C_3N_4)$$

$$BFO + hv \rightarrow h^+_{VB}(BFO) + e^-_{CB}(BFO)$$

$$e^-_{CB}(BFO) + h^+_{VB}(s\text{-}C_3N_4) \rightarrow \text{recombination}$$

$$e^-_{CB}(s\text{-}C_3N_4) + O_2 \rightarrow •O_2^-(s\text{-}C_3N_4)$$

$$h^-_{VB}(BFO) + H_2O \rightarrow •OH(BFO) + h^+$$

$$•OH(BFO) + h^+ + •O_2^-(s\text{-}C_3N_4) + MB \rightarrow \text{Degradation products}$$

The recombination between electrons (e^-) in BFO and holes (h^+) in C_3N_4 can effectively promote the separation and transfer of photo-generated electron-hole pairs. Eventually, the s-C_3N_4/BFO heterojunction exhibits excellent photocatalytic degradation ability.

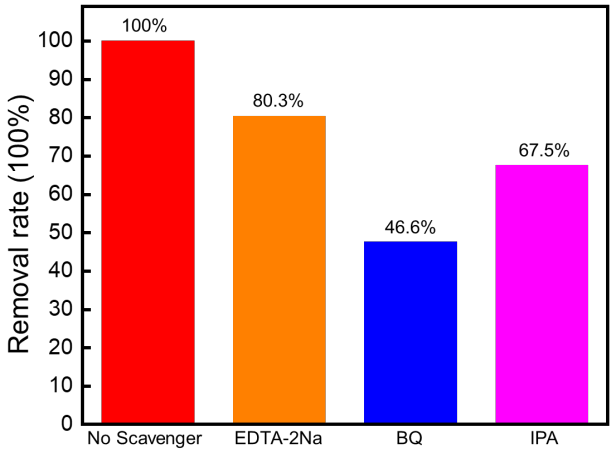

Figure 9. Capture experiment of photocatalytic degradation of MB by s-C_3N_4/BFO.

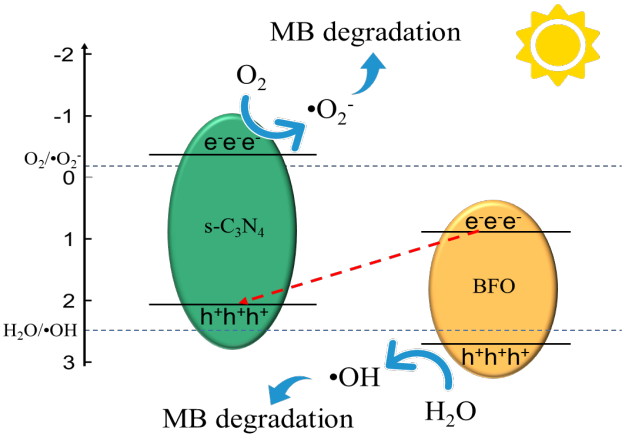

Figure 10. Schematics diagram of photocatalytic degradation by BFO/s-C_3N_4 Z-Scheme heterojunction.

4. Conclusions

In this work, we achieved the synthesis of s-C_3N_4/BFO Z-scheme heterojunction through the integration of nanocylindrical BFO and s-C_3N_4. Notably, the heterojunction exhibited superior adsorption capacity and degradation efficiency. The large specific surface area of nanocylindrical BFO facilitated the uniformly in-situ embedding on the s-C_3N_4 surface, significantly inhibiting the recombination of photogenerated carriers. Additionally, the negative potential-induced adsorption on s-C_3N_4 surface significantly contributed to the subsequent degradation process. The in-situ embedding of $Bi_{25}FeO_{40}$ within scaffold C_3N_4 promotes photogenerated carrier separation, leading to an optimized degradation rate of 0.0205 min^{-1} and a contaminant removal efficiency of 85.3%. This study presents a novel approach for sewage purification, fostering advancements in environmental protection.

Acknowledgment

We acknowledge the National Natural Science Foundation of China (Nos. 52072182 and 51872145), Graduate Research Innovation Fund of Jiangsu Province (KYCX19_0935), Nanjing Institute of Technology Scientific Research Fund (YKJ202353) and the National Synergetic Innovation Center for Advanced Materials (SICAM).

References

[1] E. Forgacs, T. Cserháti, and G. Oros, "Removal of synthetic dyes from wastewaters: A review," *Environment International*, vol. 30, no. 7, pp. 953-971, 2004.

[2] A. Houas, H. Lachheb, M. Ksibi, E. Elaloui, C. Guillard, and J.-M. Herrmann, "Photocatalytic degradation pathway of methylene blue in water," *Applied Catalysis B-Environment and Energy*, vol. 31, no. 2, pp. 145-157, 2001.

[3] C. Chen, W. Ma, and J. Zhao, "Semiconductor-mediated photo-degradation of pollutants under visible-light irradiation," *Chemical Society Reviews*, vol. 39, no. 11, pp. 4206-4219, 2010.

[4] N. Manavi, A. S. Kazemi, and B. Bonakdarpour, "The development of aerobic granules from conventional activated sludge under anaerobic-aerobic cycles and their adaptation for treatment of dyeing wastewater," *Chemical Engineering Journal*, vol. 312, pp. 375-384, 2017.

[5] G. Crini, "Non-conventional low-cost adsorbents for dye removal: A review," *Bioresour Technol*, vol. 97, no. 9, pp. 1061-085, 2006.

[6] Mohd. Rafatullah, O. Sulaiman, R. Hashim, and A. Ahmad, "Adsorption of methylene blue on low-cost adsorbents: A review," *Journal of Hazardous Materials*, vol. 177, no. 1, pp. 70-80, 2010.

[7] B.-J. Yao, W.-L. Jiang, Y. Dong, Z.-X. Liu, and Y.-B. Dong, "Post-synthetic polymerization of UiO-66-NH_2 nanoparticles and polyurethane oligomer toward stand-alone membranes for dye removal and separation," *Chemistry A European Journal*, vol. 22, no. 30, pp. 10565-10571, 2016.

[8] A. R. Bagheri, M. Ghaedi, A. Asfaram, A. A. Bazrafshan, and R. Jannesar, "Comparative study on ultrasonic assisted adsorption of dyes from single system onto Fe_3O_4 magnetite nanoparticles

loaded on activated carbon: Experimental design methodology," *Ultrasound Sonochemisty*, vol. 34, pp. 294-304, 2017.

[9] Y. Liu, C. Hou, T. Jiao, J. Song, X. Zhang, R. Xing, J. Zhou, L. Zhang, and Q. Peng, "Self-assembled AgNP-containing nanocomposites constructed by electrospinning as efficient dye photocatalyst materials for wastewater treatment," *Nanomaterials*, vol. 8, no. 1, Art. no. 1, 2018.

[10] B. Sun, G. Zhou, T. Gao, H. Zhang, and H. Yu, "NiO nanosheet/TiO_2 nanorod-constructed p–n heterostructures for improved photocatalytic activity," *Applied Surface Science*, vol. 364, pp. 322-331, 2016.

[11] B. Wang, X. Wang, H. Yuan, T. Zhou, J. Chang, and H. Chen, "Direct Z-scheme photocatalytic overall water splitting on two dimensional $MoSe_2/SnS_2$ heterojunction," *International Journal of Hydrogen Energy*, vol. 45, no. 4, pp. 2785-2793, 2020.

[12] Y. Yu, J. Zhou, Z. Guo, and Z. Sun, "Novel Two-dimensional janus $MoSiGeN_4$ and $WSiGeN_4$ as Highly efficient photocatalysts for spontaneous overall water splitting," *ACS Applied Materials & Interfaces*, vol. 13, no. 24, pp. 28090-28097, 2021.

[13] F. Albert, R. Ramamoorthy, G. Vincent, C. Fèlix, and B. Manuel, "Electrical control of magnetism by electric field and current-induced torques," *Reviews of Modern Physics*, vol. 96, no. 1, 2024.

[14] D. Pan, Y. Lu, A. M. Idris, C. Zhihao, L. Xu, J. Wang, G. Jiang, Z. Chen, and Z. Li, Enhancing photocatalytic CO_2 reduction via a single-domain ferroelectric Z-scheme heterojunction of $BiFeO_3/CsPbBr_3$ inducing dual built-in electric fields," *Journal of Materials Chemistry A*, vol. 12, no. 17, pp. 10461-10471, 2024.

[15] D. Vaz, C.-C. Lin, J. J. Plombon, W. Choi, I. Groen, I. C. Arango, A. Chuvilin, L. E. Hueso, D. E. Nikonov, H. Li, P. Debashis, S. B. Clendenning, T. A. Gosavi, Y. L. Huang, B. Prasad, R. Ramesh, A. Vecchiola, M. Bibes, K. Bouzehouane, S. Fusil, V. Garcia, L. A. Young, and F. Casanova, "Voltage-based magnetization switching and reading in magnetoelectric spin-orbit nanodevices," *Nature Communications*, vol. 15, no. 1, pp. 1902-1917, 2024.

[16] M. A. M. Salleh, D. K. Mahmoud, W. A. W. A. Karim, and A. Idris, "Cationic and anionic dye adsorption by agricultural solid wastes: A comprehensive review," *Desalination*, vol. 280, no. 1, pp. 1-13, 2011.

[17] A. O. Ibhadon, and P. Fitzpatrick, "Heterogeneous photocatalysis: Recent advances and applications," *Catalysts*, vol. 3, no. 1, 2013.

[18] M. Pelaez, N. T. Nolan, S. C. Pillai, M. K. Seery, P. Falaras, A. G. Kontos, P. S. M. Dunlop, J. W. J. Hamilton, J. A. Byrne, K. O'Shea, M. H. Entezari, and D. D. Dionysiou, "A review on the visible light active titanium dioxide photocatalysts for environmental applications," *Applied Catalysis B-Environment and Energy*, vol. 125, pp. 331-349, 2012.

[19] I. K. Konstantinou, and T. A. Albanis, "TiO_2-assisted photocatalytic degradation of azo dyes in aqueous solution: kinetic and mechanistic investigations," *Applied Catalysis B-Environment and Energy*, vol. 49, no. 1, pp. 1-14, 2004.

[20] J. Li, X. Liu, and J. Zhang, "Smart assembly of sulfide heterojunction photocatalysts with well-defined interfaces for direct z-scheme water splitting under visible light," *ChemSusChem*, vol. 13, no. 11, pp. 2996-3004, 2020.

[21] J.-H. Qin, H. Zhang, P. Sun, Y.-D. Huang, Q. Shen, X.-G. Yang, and L.-F. Ma "Ionic liquid induced highly dense assembly of porphyrin in MOF nanosheets for photodynamic therapy," *Dalton Transactions*, vol. 49, no. 48, pp. 17772-17778, 2020.

[22] J.-H. Qin, W.-J. Qin, Z. Xiao, J.-K. Yang, H.-R. Wang, X.-G. Yang, D.-S. Li, and L.-F. Ma, "Efficient Energy-transfer-induced high photoelectric conversion in a dye-encapsulated ionic pyrene-based metal–organic framework," *Inorganic Chemistry*, 2021.

[23] J. Wen, J. Xie, X. Chen, and X. Li, "A review on g-C_3N_4-based photocatalysts," *Applied Surface Science*, vol. 391, pp. 72-123, 2017.

[24] E. B. Azimi, A. Badiei, M. H. Sadr, and A. Amiri, "A template-free method to synthesize porous G-C_3N_4 with efficient visible light photodegradation of organic pollutants in water," *Advanced Powder Technology*, vol. 29, no. 11, pp. 2785-2791, 2018.

[24] Z. Liu, X. He, X. Yang, H. Ding, D. Wang, D. Ma, and Q. Feng, "Synthesis of mesoporous carbon nitride by molten salt-assisted silica aerogel for Rhodamine B adsorption and photocatalytic degradation," *Journal of Materials Science*, vol. 56, no. 19, pp. 11248-11265, 2021.

[26] S. C. Yan, Z. S. Li, and Z. G. Zou, "Photodegradation performance of g-C_3N_4 fabricated by directly heating melamine," *Langmuir*, vol. 25, no. 17, pp. 10397-10401, 2009.

[27] X. C. Wang, K. Maeda, A. Thomas, K. Takanabe, G. Xin, J. M. Carlsson, K. Domen, and M. Antonietti, "A metal-free polymeric photocatalyst for hydrogen production from water under visible light" *Nature Materials*, vol. 8, pp. 76-80, 2009.

[28] L. Ren, S. Y. Lu, J. Z. Fang, Y. Wu, D. Z. Chen, L. Y. Huang, Y. F. Chen, C. Cheng, Y. Liang, and Z. Q. Fang, "Enhanced degradation of organic pollutants using $Bi_{25}FeO_{40}$ microcrystals as an efficient reusable heterogeneous photo-Fenton like catalyst," *Catalysis Today*, vol. 281, pp. 656-661, 2017.

[29] J. Zhu, P. Xiao, H. Li, and S. A. C. Carabineiro, "Graphitic carbon nitride: Synthesis, properties, and applications in catalysis," *ACS Applied Materials & Interfaces*, vol. 6, no. 19, pp. 16449-16465, 2013.

[30] Y.-S. Xu, and W.-D. Zhang, "Ag/AgBr-grafted graphite-like carbon nitride with enhanced plasmonic photocatalytic activity under visible light," *ChemCatChem*, vol. 5, no. 8, pp. 2343-2351, 2013.

[31] Y. Guo, J. Li, Z. Gao, X. Zhu, Y. Liu, Z. Wei, W. Zhao, and C. Sun, "A simple and effective method for fabricating novel p–n heterojunction photocatalyst g-$C_3N_4/Bi_4Ti_3O_{12}$ and its photocatalytic performances," *Applied Catalysis B-Environment and Energy*, vol. 192, pp. 57-71, 2016.

[32] M. Zhu, C. Zhai, M. Sun, Y. Hu, B. Yan, and Y. Du, "Ultrathin graphitic C_3N_4 nanosheet as a promising visible-light-activated support for boosting photoelectrocatalytic methanol oxidation," *Applied Catalysis B-Environment and Energy*, vol. 203, pp. 108-115, 2017.

[33] G.-Q. Tan, Y.-Q. Zheng, H.-Y. Miao, A. Xia, and H.-J. Ren, "Controllable microwave hydrothermal synthesis of bismuth ferrites and photocatalytic characterization," *Journal of the American Ceramics Society*, vol. 95, no. 1, pp. 280-289, 2012.

[34] Y. Liu, H. Guo, Y. Zhang, W. Tang, X. Cheng, and W. Li, "Heterogeneous activation of peroxymonosulfate by sillenite Bi25FeO40: Singlet oxygen generation and degradation for aquatic levofloxacin," *Chemical Engineering Journal*, vol. 343, pp. 128-137, 2018.

[35] L. Zhang, X. Zhang, Y. Zou, Y-H. Xu, C. Pan, J-S. Hu, and C-M. Hou, "Hydrothermal synthesis, influencing factors and excellent photocatalytic performance of novel nanoparticle-assembled $Bi_{25}FeO_{40}$ tetrahedrons," *CrystEngComm*, vol. 17, no. 34, pp. 6527-6537, 2015.

[36] L. Wu, C. Dong, H. Chen, J. Yao, C. Jiang, and D. Xue, "Hydro-thermal synthesis and magnetic properties of bismuth ferrites nanocrystals with various morphology," *Journal of the American Ceramic Society*, vol. 95, no. 12, pp. 3922-3927, 2012.

[37] Y. Wu, H. Luo, X. Jiang, H. Wang, and J. Geng, "Facile synthesis of magnetic $Bi_{25}FeO_{40}$/rGO catalyst with efficient photocatalytic performance for phenolic compounds under visible light," *RSC Advances*, vol. 5, no. 7, pp. 4905-4908, 2014.

[38] W. Ji, M. Li, G. Zhang, and P. Wang, "Controlled synthesis of $Bi_{25}FeO_{40}$ with different morphologies: Growth mechanism and enhanced photo-fenton catalytic properties," *Dalton Transacations*, vol. 46, no. 32, pp. 10586-10593, 2017.

[39] L. Yang, W. Yang, S. Liang, Z. Lin, J. Pan, and C. Yang, "Insight into the in-situ surface reconstruction of perovskite $BiFeO_3$ for boosting nitrate electroreduction to ammonia," *Applied Catalysis B-Environment and Energy*, vol. 349, p. 123864, 2024.

[40] M. G. Abdelkader, N. F. Atta, and A. Galal, "Boosting the charge for the selective photoelectrochemical oxidation of hydroquinone in hazardous environments using a fine-tuned heterojunction catalyst," *Journal of Materials Chemistry A* , vol. 12, no. 16, pp. 9606-9626, 2024.

[41] M. Ai, J.-W. Zhang, R. Gao, L. Pan, X. Zhang, and J.-J. Zou, "MnOx-decorated 3D porous C_3N_4 with internal donor–acceptor motifs for efficient photocatalytic hydrogen production," *Applied Catalysis B-Environment and Energy*, vol. 256, p. 117805, 2019.

[42] A. N. Kadam, M. Moniruzzaman, and S.-W. Lee, "Dual functional s-doped g-C_3N_4 pinhole porous nanosheets for selective fluorescence sensing of Ag^+ and visible-light photocatalysis of dyes," *Molecules*, vol. 24, no. 3, 2019.

[43] G. Fu, W. Li, H. Cao, X. Chen, S. Wang, L. Luo, M. Wu, H. Tian, Z. Ren, and G. Han, "Polarization screening-induced epitaxial growth and interfacial magnetism of $BiFeO_3$/$PbTiO_3$ nanoplates," *CrystEngComm*, vol. 22, no. 4, pp. 639-645, 2020.

[44] R. Bibi, L. Wei, Q. Shen, W. Tian, O. O. Kehinde, N. Li, and J. Zhou "Effect of Amino Functionality on the uptake of cationic dye by titanium-based metal organic frameworks," *Journal of Chemical & Engineering Data*, vol. 62, no. 5, pp. 1615-1622, 2017.

[45] A. Sun, H. Chen, C. Song, F. Jiang, X. Wang, and Y. Fu, "Magnetic $Bi_{25}FeO_{40}$-graphene catalyst and its high visible-light photocatalytic performance," *RSC Advances*, vol. 3, no. 13, pp. 4332-4340, 2013.

[46] M. M. de Góis, W. de Paiva Araújo, R. B. da Silva, G. E. da Luz, and J. M. Soares, "$Bi_{25}FeO_{40}$–Fe_3O_4–Fe_2O_3 composites: Synthesis, structural characterization, magnetic and UV–visible photocatalytic properties," *Journal of Alloys and Compounds*, vol. 785, pp. 598-602, 2019.

[47] Y. Wang, Y. Di, M. Antonietti, H. Li, X. Chen, and X. Wang, "Excellent visible-light photocatalysis of fluorinated polymeric carbon nitride solids," *Chemistry of Materials*, vol. 22, no. 18, pp. 5119-5121, 2010.

[48] X. Li, Y. Qiu, Z. Zhu, H. Zhang, and D. Yin, "Novel recyclable Z-scheme g-C_3N_4/carbon nanotubes/$Bi_{25}FeO_{40}$ heterostructure with enhanced visible-light photocatalytic performance towards tetracycline degradation," *Chemical Engineering Journal*, vol. 429, p. 132130, 2022.

[49] P. Raizada, A. Sudhaik, S. Patial, V. Hasija, A. A. P. Khan, P. Singh, S. Gautam, M. Kaur, and V-H. Nguyen, "Engineering nanostructures of CuO-based photocatalysts for water treatment: Current progress and future challenges," *Arabian Journal of Chemistry*, vol. 13, no. 11, pp. 8424-8457, 2020.

[50] S. A. Behera, A. Amanat, and P. G. R. Achary, "Photocatalytic degradation of ciprofloxacin drug utilizing novel PVDF/ polyaniline/lanthanum strontium manganate@Ag composites," *Journal of Metals, Materials Minerials*, vol. 34, no. 1, 2024.

[51] B. Dai, C. Gao, J. Guo, M. Ding, Q. Xu, S. He, Y. Mou, H. Dong, M. Hu, Z. Dai, Y. Zhang, Y. Xie, and Z. Lin, "A robust pyro-phototronic route to markedly enhanced photocatalytic disinfection," *Nano Letters*, vol. 24, no. 16, pp. 4816-4825, 2024.

[52] B. Dai, J. Guo, C. Gao, H. Yin, Y. Xie, and Z. Lin, "Recent advances in efficient photocatalysis via modulation of electric and magnetic fields and reactive phase control," *Advanced Materials*, vol. 35, no. 14, p. 2210914, 2023.

[53] L. Sahoo, S. A. Behera, R. K. Singh, S. K. Parida, and P. G. R. Achary, "Microstructural and dielectric characteristics of the Ce-doped Bi_2FeMnO_6," *Journal of Metals, Materials and Minerals*, vol. 34, no. 1, 2024,.

[54] N. Saechin, S. Sripho, T. Rattanawongwiboon, S. Laksee, P. Lertsarawut, W. Kingkam, S. Ummartyotin, "Synthesis and modification of nickel hydroxide particle synthesized by self-assembly and electron beam irradiation technique for photocatalyst activity," *Journal of Metals, Materials and Minerals*, vol. 33, no. 4, 2023.

[55] W. Promsuwan, P. Sujaridworakun, and W. Reainthippayasakul, "Synthesis of zinc oxide photocatalysts from zinc-dust waste for organic dye degradation," *Journal of Metals, Materials and Minerals*, vol. 33, no. 2, 2023.